International Journal of Pharmaceutics 497 (2016) 210–221

Contents lists available at ScienceDirect

International Journal of Pharmaceutics

journal homepage: www.elsevier.com/locate/ijpharm

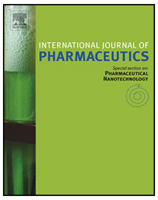

Nanocomposite hydrogel incorporating gold nanorods and paclitaxel-loaded chitosan micelles for combination photothermal–chemotherapy

Nan Zhang, Xuefan Xu, Xue Zhang, Ding Qu, Lingjing Xue*, Ran Mo, Can Zhang*

State Key Laboratory of Natural Medicines and Jiangsu Key Laboratory of Drug Discovery for Metabolic Diseases, Center of Drug Discovery, China Pharmaceutical University, Nanjing 210009, China

A R T I C L E I N F O

Article history:
Received 29 June 2015
Received in revised form 5 November 2015
Accepted 16 November 2015
Available online 1 December 2015

Keywords:
Photothermal therapy
Chemotherapy
Gold nanorod
Chitosan micelles
Combination therapy

A B S T R A C T

Development of combination photothermal–chemotherapy platform is of great interest for enhancing antitumor efficacy and inhibiting tumor recurrence, which supports selective and dose-controlled delivery of heat and anticancer drugs to tumor. Here, an injectable nanocomposite hydrogel incorporating PEGylated gold nanorods (GNRs) and paclitaxel-loaded chitosan polymeric micelles (PTX-M) is developed in pursuit of improved local tumor control. After intratumoral injection, both GNRs and PTX-M can be simultaneously delivered and immobilized in the tumor tissue by the thermo-sensitive hydrogel matrix. Exposure to the laser irradiation induces the GNR-mediated photothermal damage confined to the tumor with sparing the surrounding normal tissue. Synergistically, the co-delivered PTX-M shows prolonged tumor retention with the sustained release of anticancer drug to efficiently kill the residual tumor cells that evade the photothermal ablation due to the heterogeneous heating in the tumor region. This combination photothermal–chemotherapy presents superior effects on suppressing the tumor recurrence and prolonging the survival in the Heps-bearing mice, compared to the photothermal therapy alone.

1. Introduction

Nanotechnology-based photothermal ablation (PTA) has been intensively explored as a minimally invasive treatment for solid tumors in recent years. This technique using the photothermal nanostructures, such as gold nanoshells, gold nanorods (GNRs), gold nanocages and carbon nanotubes as strong optical absorbers to convert harmless near infrared (NIR) light into localized heat, holds great promise to achieve selective and confined thermal damage within tumor while minimizing damage to the surrounding healthy tissue and preserving critical structures (Huang et al., 2008; Qin and Bischof, 2012; Shanmugam et al., 2014; Thakor and Gambhir, 2013). The gold nanoshells mediated PTA to treat refractory head and neck cancer is currently undergoing in clinical trial (Singh and Torti, 2013). GNRs have also received considerable attention due to their efficient large-scale synthesis, facile bioconjugation, strong and tunable plasmonic absorption (Chen et al., 2013a; Dickerson et al., 2008; Huang et al., 2009; Vigderman et al., 2012; von Maltzahn et al., 2009). The efficacy of tumor-specific thermal damage is highly dependent on the tumor-specific accumulation and localization of photothermal nanostructures following intravenous or local administration (Kennedy et al., 2011; Shenoi et al., 2011; Soni et al., 2014; Xu et al., 2013). Intravenously injected photothermal nanoparticles are known to be preferentially delivered to tumor *via* passive or active targeting mechanism, but their dynamic concentration and distribution in tumor fluctuate in terms of various factors associated with particle characteristics and physiological barriers, posing problems in nanoparticle dosimetry to obtain a reproducible heating profile in PTA (Alkilany et al., 2012; Chauhan et al., 2011; Khlebtsov and Dykman, 2011; Wicki et al., 2015). Local administration affords preferable nanoparticle dose control for PTA, but may be compromised by the rapid diffusion and distant migration of photothermal nanostructures away from tumor, inability to distribute throughout the whole tumor due to pressure gradient and matrix constraint within tumor (Le Renard et al., 2010; Meenach et al., 2010; Mooney et al., 2014; Redolfi Riva et al., 2014). A single dose of PTA may be difficult to achieve complete ablation due to the heterogeneous heat distribution caused by uneven distribution of photothermal nanostructures, the gradual attenuation of NIR light energy as it travels deeper into tissue, highly

---

* Corresponding authors. Fax: +86 25 83271171.
E-mail addresses: xuelingjing65@163.com (L. Xue), zhangcan@cpu.edu.cn (C. Zhang).

http://dx.doi.org/10.1016/j.ijpharm.2015.11.032

variable local tissue factors, including location, geometries of tumor, optical and thermal properties of tissue, and heat sink effect (Bhatia et al., 2010; Lu et al., 2011; Oliva et al., 2015; Ren et al., 2013).

The potential risk of incomplete photothermal ablation often results in local tumor recurrence, which requires an alternative therapeutic intervention to achieve the completeness of tumor ablation. The combination of thermal ablation with chemotherapy that is increasingly adopted in the experimental and clinical levels has been demonstrated able to increase intratumoral drug accumulation, tumor destruction volume within the peripheral zone of sub-lethal temperature, and improve antitumor efficacy (Ahmed et al., 2012; Issels, 2008; Li et al., 2014; Sun et al., 2014). In addition, a sustained and localized chemotherapy offers many advantages of allowing accurate dosage and one-time administration, facilitating efficient delivery of anticancer agents, reducing the systemic toxicity, prolonging drug exposure, and ensuring more cytotoxic to tumors cells over multiple cell cycles (Mo et al., 2014; Weinberg et al., 2008; Wolinsky et al., 2012).

Herein, we report an injectable hydrogel incorporating photothermal nanostructures and chemotherapeutics for combined PTA and localized chemotherapy to achieve controlled and selective thermal tumor damage with reduced the risk of local recurrence and systemic cytotoxicity (Fig. 1). This nanocomposite hydrogel (designated as PTX/GNR/gel) co-encapsulates PEGylated (PEG = polyethylene glycol) GNRs and paclitaxel (PTX)-loaded chitosan polymeric micelles (PTX-M) in a thermal-reversible Poly(F127) hydrogel matrix, in which both of the PEGylated GNRs and PTX-M could be homogeneously mixed on a demand basis. The PEGylated GNRs with the superior colloidal stability serve as photothermal transducer to convert the NIR light energy into heat to destroy tumor. The strength of the heat can be readily tailored by adjusting the amount of the PEGylated GNRs and the power intensity of the NIR laser. A synthetic amphiphilic chitosan derivative is used to load PTX, a model chemotherapeutic for treatment of many types of cancer, and then incorporated into the hydrogel matrix, which can prevent the precipitation of PTX that causes a poor dose control and uneven drug distribution in the matrix. The polymeric hydrogel matrix also renders a longer retention capacity of PTX-M at the tumor site, compared to the flowable solution without the hydrogel support. After intratumoral injection, PTX-M/GNR/gel is immobilized in the tumor region due to the thermal gelling properties of the Poly(F127) polymer. Under NIR laser irradiation, the heat generated by the GNR-mediated photothermal conversion was confined within tumor. Following the photothermal treatment, PTX-M/GNR/gel as a localized drug depot could liberate PTX-M into the tumor tissue, which plays an important role in eradicating the potential remaining viable tumor cells, thereby achieving an improved completeness of tumor destruction. Such a synergistic effect of photothermal–chemotherapy would finally contribute to a reduction and delay of tumor recurrence.

2. Material and methods

2.1. Materials

Cetyltrimethyl ammonium bromide (CTAB) was purchased from NanShi Chemical Reagent Co., Ltd. (Jiangsu, China). Tetrachloroaurate (III) acid hydrate ($HAuCl_4 \cdot 4H_2O$) were purchased from Sinopharma Group Co., Ltd. (Shanghai, China). mPEG-SH (MW 5 kDa) was purchased from Sinopeg Biotech Co., Ltd. (Xiamen, China). Chitosan with deacetylation degree of 92% and viscosity average molecular weight of 70 KDa was purchased from Shuangling Biochemical Co., Ltd. (Nantong, China). PTX was purchased from Yew Pharmaceutical Company Ltd. (Jiangsu, China). F127 was provided by Badische Anilin and Soda-Fabrik (BASF). Stannous 2-ethyl-hexanoate ($SnOct_2$) and hexamethylene diisocyanate (HDI) were purchased from Aladdin Reagent Company (Shanghai, China).

2.2. Synthesis and characterization of PEGylated GNRs

CTAB-stabilized GNRs (CTAB-GNRs) were synthesized using a seed-mediated silver ion-assisted growth method (Ni et al., 2008). PEGylation of GNRs was performed as previous described (Liao and Hafner, 2005). In brief, mPEG-SH was added into a concentrated CTAB-GNRs solution to a final concentration of 10 mM, and the pH of the mixture was adjusted to 8.5 by K_2CO_3 (0.1 M). The mixture was sonicated for 4 h and incubated overnight, followed by two cycles of centrifugation–redispersion in deionized (DI) water.

The absorption spectra of GNRs were determined using a spectrophotometer (UV-5300, Metash, China), and the dimensions

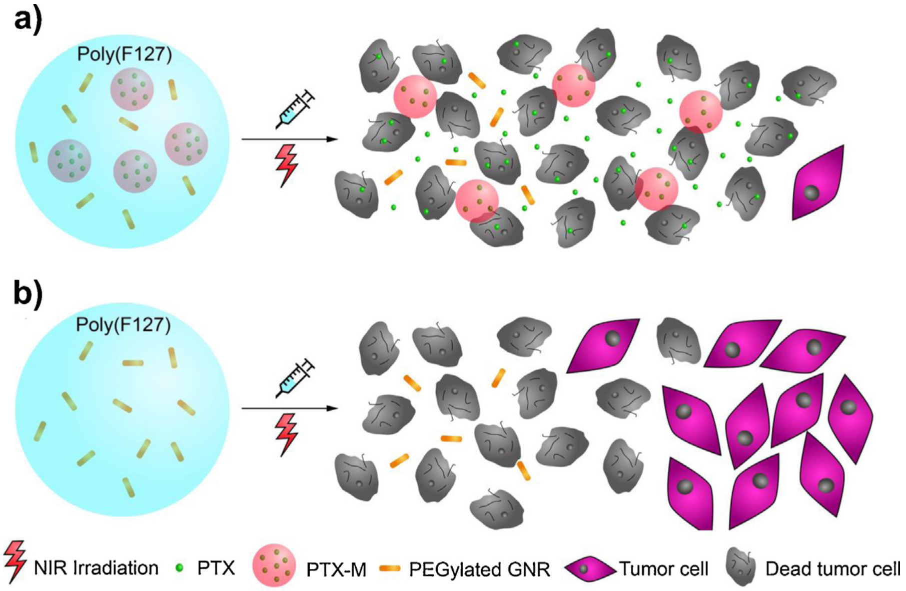

Fig. 1. Schematic design of the PTX-M/GNR/gel mediated photothermal–chemotherapy (a) for enhancing antitumor efficacy and inhibiting tumor recurrence compared to the GNR/gel mediated photothermal ablation alone (b).

and aspect ratios of GNRs were measured based on TEM (Hitachi-7650). The zeta potentials of GNRs were assayed using a zeta potential analyzer (ZetaPlus, Brookhaven). The Au concentration in GNRs solution was determined by an inductively coupled plasma-mass spectrometry (ICP–MS, PerkinElmer).

2.3. Synthesis and characterization of N-octyl-N,O-succinyl-O-phosphoryl chitosan (OSPC)

N-octyl chitosan (OC) was synthesized by introducing the octyl group to NH_2 of glucosamine in the chitosan as previous described (Yao et al., 2007).

Succinic anhydride (3.27 g, 32.7 mmol) was added to 80 mL of the OC (8.05 g, 32.7 mmol) DMF solution under nitrogen atmosphere, and the mixture was stirred at 90 °C for 6 h. The reaction mixture cooled to room temperature, and *N*-octyl-*N*,*O*-succinyl chitosan (OSC) was precipitated by the addition of 270 mL of water. The filtered OSC was washed repeatedly with water, followed by freeze-drying.

Phthalic anhydride (1.9 g) dissolved in 3 mL of DMF was added dropwise into 4 mL of the OSC (1 g, 3.7 mmol) DMF solution with stirring at 35 °C. The mixture was heated up to 70 °C slowly, and stirred for another 5 h. The reaction mixture was diluted with DI water, neutralized by NaOH solution, and dialyzed (MWCO 10 kDa) against DI water for 3 days. OSPC was obtained as a gold-yellow powder by freeze-drying, and was characterized by FT-IR and ^{1}H NMR. The substitution degrees of octyl and succinyl groups were determined by the elemental analysis, while that of phosphoryl group was quantified by the colorimetric phosphate assay.

2.4. Preparation and characterization of micelles

PTX-loaded OSPC micelle (PTX-M) was prepared by the dialysis method (Jin et al., 2014; Mo et al., 2011). Briefly, PTX (9.6 mg) dissolved in 0.2 mL of ethanol was added into 2 mL of OSPC (16 mg) aqueous solution with stirring at room temperature. The mixture was dialyzed (MWCO 10 kDa) against DI water for 8 h, and filtrated through a 0.45 μm pore-sized membrane. Taxol, the commercial PTX formulation, was prepared by dissolving PTX into the mixture of Cremophor EL and ethanol (50/50, v/v) at a concentration of 6 mg/mL.

For fluorescence-based imaging or assay, DiR and PTX co-loaded micelle (DiR/PTX-M) and FRET micelle (FRET-M) containing PTX, DiO and DiI were prepared. Briefly, 8 μL of the DiR DMSO solution (2 mg/mL) and DiO/DiI (1/1, w/w, DiO/PTX = 0.52%) was added into the PTX ethanol solution, respectively. Other steps were identical to the PTX-M preparation described above. DiR-labeled Taxol (DiR/Taxol) was prepared by adding 5 μL of the DiR DMSO solution to 1 mL of the Taxol formulation.

The CMC of OSPC was determined using a pyrene-based method (Wiradharma et al., 2008). The fluorescence spectrum of pyrene was measured using a fluorophotometer (RF-5301 PC, Shimadzu) with 334 nm excitation. The CMC of OSPC was calculated from the intersection of two tangent plots intensity ratio (I_{383}/I_{373}) against the log concentration of OSPC.

The hydrodynamic diameter and zeta potential of the micelles were measured using a Dynamic Light Scattering Analyzer (ZetaPlus, Brookhaven). The morphology of PTX-M was observed using TEM (H-7650, Hitachi) with phosphotungstic acid staining at an accelerating voltage of 80 kV.

The quantity of PTX in PTX-M was determined using HPLC system (Agilent 1100 series) equipped with a reverse-phase column (Intersil® ODS-SP, 4.6 × 150 mm). The mobile phase consisted of methanol and water (75/25, v/v) was delivered at a flow rate of 1.0 mL/min. The detection wavelength was 227 nm, and the injection volume was 20 μL. The PTX-M solution was disrupted with methanol prior to HPLC analysis. The entrapment efficiency ($W_{PTX}/W_0 \times 100\%$) and the drug-loading capacity ($W_{PTX}/(W_{PTX} + W_{OSPC}) \times 100\%$) were calculated, where W_{PTX}, W_0 and W_{OSPC} are the quantities of PTX in the micelles, the feeding PTX and OSPC in the micelles, respectively.

2.5. In vitro cytotoxicity

HepG2 cells were obtained from the Cell Bank of Chinese Academy of Sciences (Shanghai, China) and were maintained in the DMEM medium supplemented with 10% (v/v) fetal bovine serum and 1% penicillin-streptomycin at 37 °C in 5% CO_2.

The *in vitro* cytotoxicity of PTX formulations and corresponding blank carriers was evaluated against HepG2 cells by the MTT assay. In brief, approximately 5000 cells per well were precultured in 96-well plates for 24 h. The cells were then incubated with 200 μL of the following test solutions for 48 h: (1) PTX-M; (2) Taxol; (3) free PTX; (4) bare OSPC micelles; (5) bare Taxol vehicle. The free PTX solution was prepared by dissolving certain amount of PTX in DMEM medium containing 1.67% DMSO. The drug-free carriers (bare OSPC and Taxol vehicle) were diluted as the same fold as their corresponding PTX formulations. After incubation, 20 μL of MTT (5 mg/mL) was added into each well, followed by an additional 4 h of incubation. The solution was replaced by 150 μL of DMSO to dissolve the formed formazan crystals. Cell viability (%) was calculated by comparing the absorbance at 570 nm of testing wells with the control wells containing untreated cells.

2.6. Preparation and characterization of nanocomposite hydrogel

Poly(F127) was synthesized by polymerizing the triblock copolymer PEO–PPO–PEO (F127) with HDI as described previously (Chen et al., 2013b), and was characterized by FT-IR.

PTX-M/GNR/gel incorporating PEGylated GNRs and PTX-M was prepared by the "cold method" (Lin et al., 2014). In brief, the PEGylated GNRs suspension was centrifuged at 10,000 g for 20 min, and the pellet was resuspended with the PTX-M solution. Afterward, the Poly(F127) powder was dissolved in the PTX-M/GNR mixture to a concentration of 15 wt% at 4 °C overnight. As-prepared hydrogels were stored at room temperature.

The sol-gel transition behavior of the hydrogel was determined by the test tube inverting method (Liu et al., 2007).

The rheological measurements were performed on a RS600 RheoStress rheometer (ThermoHaake, Germany) equipped with a PP60 Ti sensor (0.5 mm gap). Oscillatory temperature sweeps were performed at a frequency of 1 Hz and a strain of 0.1%. The storage modulus G' and loss modulus G'' were recorded at temperature from 10 °C to 37 °C at a heating rate of 1 °C/min.

The mechanical property of the hydrogel was measured using a texture analyzer (TA-XT2, Stable Micro Systems, Surrey, UK). Hydrogel was incubated at 37 °C to complete gelation, and the analytical probe (5 mm diameter) compressed the hydrogel to the depth of 3 mm at a constant speed of 1 mm/s. All tests were run four times for each sample.

2.7. Thermal stability of micelles

The PTX leakage from PTX-M under hyperthermic condition was investigated. In brief, PTX-M solution (1.5 mg/mL PTX) was incubated at different temperatures (50, 60, 70 °C). At predetermined time interval, the remaining encapsulated PTX in PTX-M was quantified using HPLC.

The TEM examination was applied to evaluate the stability of PTX-M after laser irradiation. 0.5 mL of PTX-M/GNR/gel (43.2 μg/mL Au) in gel phase was irradiated with 808 nm laser at a power intensity of 2 W/cm^2 for 10 min. The treated PTX-M/GNR/gel was diluted 10 times with the DI water in ice bath. The sample was stained with phosphotungstic acid for TEM observation.

The FRET-based assay was used to investigate the photothermal effect on the integrity of PTX-M in the hydrogel (Chen et al., 2008). 0.5 mL of FRET-M/GNR/gel (43.2 μg/mL Au) in gel phase was irradiated with 808 nm laser at a power intensity of 2 W/cm^2 for 10 min, and diluted 40 times with DI water in ice bath. The fluorescence spectra of FRET-M in various solvents were measured using the fluorophotometer with 484 nm excitation. The FRET ratio ($I_{\mathrm{DiI}}/(I_{\mathrm{DiI}}+I_{\mathrm{DiO}})$) was calculated, where I_{DiI} and I_{DiO} are the fluorescence intensities at 570 nm and 502 nm, respectively.

2.8. Animals and xenograft tumor models

The ICR mice (male, 18–22 g) were purchased from the College of Veterinary Medicine at Yangzhou University (Jiangsu, China). All

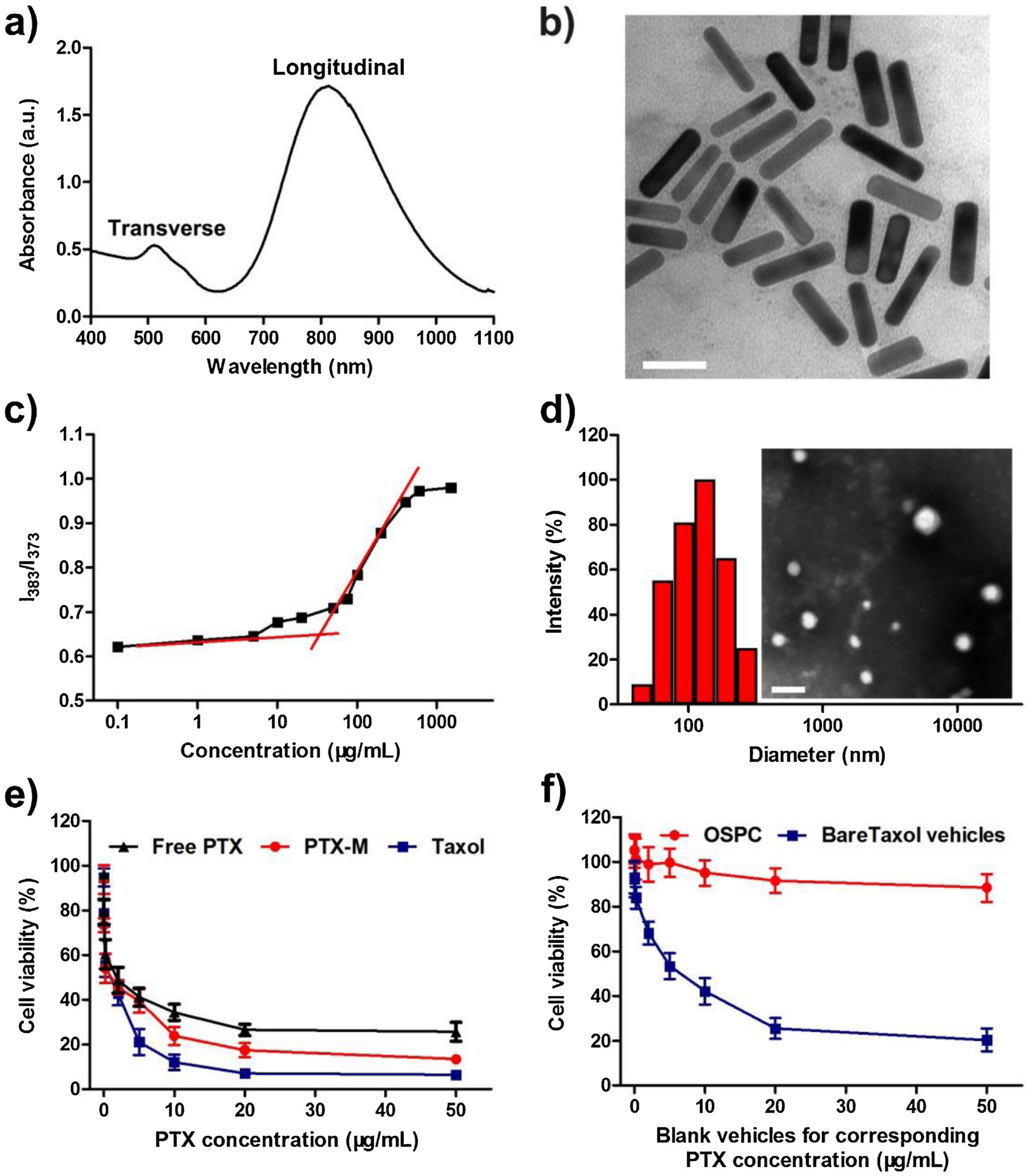

Fig. 2. (a) Absorption spectrum of the PEGylated GNRs. (b) TEM image of the PEGylated GNRs. Scale bar: 50 nm. (c) I_3/I_1 ratio of pyrene as a function of the OSPC concentration. (d) Particle size distribution of PTX-M determined by the dynamic light scattering. Inset: TEM image of PTX-M. Scale bar: 200 nm. (e) Viability of HepG2 cells after 48 h of incubation with Taxol, PTX-M, and free PTX ($n = 3$). (f) Viability of HepG2 cells after 48 h of incubation with the blank vehicles (OSPC and bare Taxol vehicles) for corresponding PTX concentration varies from 0.002 to 50 μg/mL ($n = 3$).

the animal experiments were conducted in compliance with the Guide for Care and Use of Laboratory Animals, approved by China Pharmaceutical University. To establish the xenograft tumor model, 0.2 mL of the murine hepatocellular carcinoma (Heps) cells (2×10^7 cell/mL) in PBS were subcutaneously innoculated in the right axillary region of the mice. The tumor volume ($L \times W^2/2$) was monitored and determined, where L and W are the length and width of the tumor, respectively. The Heps-bearing mice were used in the following experiments when the tumor volume reached about 300–400 mm^3.

2.9. In vivo *photothermal conversion characteristics*

The Heps-bearing mice were intratumorally injected with PTX-M/GNR/gel (21.6– 86.4 μg/mL Au), and saline as a negative control. The entire tumor region was then irradiated with 808 nm laser at a power intensity of 1.34 or 2 W/cm^2 for 10 min. Temperature change inside the tumor was monitored by a 0.5 mm K-type thermocouple (WRNK-191) placed in the tumor center. Temperature distribution on the surface was imaged using an infrared thermographic camera (SC3000, Flirsystem, USA).

2.10. In vivo *NIR imaging and FRET imaging*

In NIR imaging study, the Heps-bearing mice were intratumorally injected with DiR/Taxol, DiR/PTX-M/gel and DiR/PTX-M/GNR/gel at DIR dose of 36 μg/kg, respectively. For DiR/PTX-M/GNR/gel (43.2 μg/mL Au), the entire tumor region was exposed to 10 min of 2 W/cm^2 laser irradiation after injection. At 0, 1, 5, 8, 12, 16 days post treatment, NIR images of the mice were captured using a Maestro *in vivo* imaging system (Cambridge Research & Instrumentation, USA). The fluorescence intensity of the tumor region was analyzed by the Maestro 3.0.0 software.

In FRET imaging study, the Heps-bearing mice were intratumorally injected with FRET-M, FRET-M/gel and FRET-M/GNR/gel. For FRET-M/GNR/gel (43.2 μg/mL Au), the entire tumor region was exposed to 10 min of 2 W/cm^2 laser irradiation. At 0, 1, 5 day after treatment, tumors were harvested, followed by cryotomy. The tumor sections were stained with Hoechst 33342 (5 μg/mL) and rinsed with PBS. The fluorescence images in nuclei channel (ex: 405 nm, em: 409–475 nm) and FRET channels (ex: 484 nm, em: 500–530 nm for DiO, 555–655 nm for DiI) were taken using CLSM (TCS SP5, Leica).

2.11. In vivo *antitumor efficacy*

The Heps-bearing mice were intratumorally injected with saline, Taxol, PTX-M/gel, GNR/gel, PTX-M/GNR/gel, respectively. Formulations containing PTX were administered at a dose of 20 mg/kg. For GNR/gel and PTX-M/GNR/gel, the Au concentration was 43.2 μg/mL, and the entire tumor region was exposed to 10 min of 2 W/cm^2 laser irradiation. The day of treatment was designated as day 0. The mice were weighed and the tumor size was measured by a caliper every other day during treatment. The survival time of each mice group was also monitored.

2.12. Histological analysis

2,3,5-triphenyltetrazolium chloride (TTC) staining was used to detect early-stage tissue changes in response to thermal ablation (Yang et al., 2010). Tumor slices (~2 mm thick) were rinsed with saline and incubated with 2% TTC solution at 37 °C for 30 min. Viable tumor tissue with intact mitochondrial enzyme activity turned red, while ablated tissue retained its original color.

For hematoxylin and eosin (HE) staining, tumors were harvested, fixed in 10% formalin and paraffin embedded. The tumor sections (6 μm) were HE stained and observed using an optical microscope (FV1100, Olympus) at 200× magnification.

2.13. Safety evaluation of OSPC/GNR/gel

OSPC/GNR/gel was prepared identical to the preparation of PTX-M/GNR/gel except that bare OSPC micelles was incorporated instead of PTX-M.

In vitro safety of OSPC/GNR/gel was evaluated against HepG 2 cells and L02 cells by the MTT assay. The testing solution was prepared by diluting OSPC/GNR/gel with DMEM complete medium in ice bath, and the folds of dilution was identical to that of the PTX formulation as described in *in vitro* cytotoxicity part.

In vivo safety of OSPC/GNR/gel was evaluated in the ICR mice. OSPC/GNR/gel was injected into the dorsal subcutaneous region of the mice. At predetermined time intervals (1, 2, 4 weeks), the mice were sacrificed, and the main organs (heart, liver, spleen, lung, kidneys and the skin tissues at the injection site) were harvested for histological examination using HE staining.

2.14. Data analysis

Results are expressed as mean ± standard deviation. Statistical significance was analyzed using the two-tailed Student's *t*-test or one-way ANOVA. Statistical significance was set at $^*P < 0.05$.

3. Results and discussion

3.1. Synthesis and characterization of the PEGylated GNRs

The CTAB-GNRs were synthesized using a seed-mediated growth method (Ni et al., 2008). The CTAB-GNRs had an aspect ratio of 4.15 with approximately 54 nm in length and 13 nm in width determined by TEM examination (Supplementary Fig. S1), which exhibited a longitudinal plasmon peak at ~810 nm. The zeta potential of the CTAB-GNRs was about +40 mV due to the presence of the highly positive charged CTAB bilayers on the GNR surface. To reduce CTAB cytotoxicity of the CTAB-GNRs and increase the stability of GNRs, the PEGylated GNRs were obtained using a ligand-exchange method with mPEG-SH based on the high interaction between the Au and thiol groups (Liao and Hafner, 2005). The surface charge of the PEGylated GNRs was about −4 mV, suggesting the successful PEGylation on the GNR surface. No significant change in the longitudinal plasmon peak was determined (Fig. 2a). The morphology of the PEGylated GNRs was characterized by the TEM imaging, which had an aspect ratio of 4.0 (Fig. 2b). The Au concentration in the PEGylated GNRs with one optical density (OD) at wavelength of 810 nm was determined to be 21.6 μg/mL using the inductively coupled plasma mass spectrometry (ICP–MS).

3.2. Preparation, characterization and in vitro *cytotoxicity of PTX-M*

To develop a water-soluble and high PTX loading vehicle, a chitosan amphiphilic derivative, OSPC was synthesized by introducing the succinyl and phosphoryl groups as hydrophilic moieties and octyl groups as hydrophobic moieties to the chitosan backbone (Supplementary Fig. S2a). The substitution degrees of the octyl and succinyl groups were determined to be 0.6 and 0.4 by the elemental analysis, respectively, while that of the phosphoryl group was quantified to be 1.07 by colorimetric phosphate assay. The chemical structure of OSPC was confirmed by ^1H NMR and FT-IR (Supplementary Fig. S2b,c). The solubility of OSPC in water was more than 25 mg/mL, and the critical micelle concentration (CMC) of OSPC was estimated to be 33 μg/mL using a pyrene-based fluorescent method (Fig. 2c) (Wiradharma et al., 2008).

To evaluate the PTX loading capacity of OSPC, different PTX-M formulations were obtained by varying the feeding weight ratio of PTX to OSPC using a dialysis method (Jin et al., 2014; Mo et al., 2011), and the drug-loading capacity and encapsulation efficiency as well as the particle size and zeta potential were measured (Supplementary Table S1). PTX-M at the feeding ratio of 0.6 was selected for the following studies, which had the drug-loading capacity of 34.8% and the encapsulation efficiency of 89%. PTX-M exhibited a zeta potential of −24 mV, and a unimodal and narrow particle size distribution with an average particle size of 128 nm and polydispersity index (PDI) of 0.184. The TEM examination showed the spherical structures of PTX-M (Fig. 2d).

The *in vitro* cytotoxicity of PTX-M and the blank OSPC micelles were evaluated against HepG2 cells using the MTT assay (Fig. 2e,f). As shown in Fig. 2e, all the PTX formulations including the free PTX, PTX-M and the commercial Taxol induced a dose-dependent inhibition on the cell viability, the half maximal inhibitory concentration (IC50) of which was about 1.39, 0.59 and 0.39 μg/mL, respectively, indicating that both PTX-M and Taxol exhibited more cytotoxic than the free PTX. However, the increased cytotoxicity of Taxol at high concentrations was ascribed partly to the significant cytotoxicity of the bare Taxol vehicles without PTX consisting of Cremophor EL and ethanol (50/50, v/v) (Fig. 2f). In sharp contrast, OSPC was found to hardly affect the cell viability in tested PTX concentration range, which suggested that the OSPC micelles acted as cytocompatible carriers for PTX and the cytotoxicity of PTX-M was mainly due to the bioactivity of PTX released from the micelles.

3.3. Preparation and characterization of nanocomposite hydrogel

Poly(F127) was synthesized as described in the previous report (Chen et al., 2013b). The structure was confirmed by FT-IR, in which the peak at 1716 cm^{-1} attributed to the urethane bond (Supplementary Fig. S3).

The sol-gel transition temperature of the Poly(F127) hydrogel was determined using a test tube inverting method (Fig. 3a) (Liu et al., 2007). The sol–gel transition temperature of the Poly(F127) hydrogel decreased from 39 °C to 20 °C as the Poly(F127) concentration increased from 5 to 20 wt%. The mechanical strength of the Poly(F127) hydrogel at different concentrations was measured at 37 °C in comparison with the F127 hydrogel at 20 wt% (Supplementary Fig. S4a). The hardness of the Poly(F127) hydrogel at 20 wt% and 15 wt% was 11.5 and 4.3 times higher than that of the F127 hydrogel, respectively. The Poly(F127) hydrogel with higher mechanical strength is expected to facilitate adequate tumor casting during intratumoral injection and prolong drug retention *in vivo*. However, the Poly(F127) hydrogel at 20 wt% became very viscous as the temperature increased, which greatly limited its syringeability. Hence, the Poly(F127) hydrogel at 15 wt% with improved mechanical strength and acceptable injectability was chosen for the following experiments.

The thermo-responsive behavior of Poly(F127) was further confirmed using the rheological temperature sweep test. As shown in Fig. 3b, both of the storage modulus (G′) and loss modulus (G″) of the Poly(F127) solution at 15 wt% was less than 50 Pa at the temperature below 20 °C, indicating that the solution remained a flowable liquid for injection. With the temperature increase, the Poly(F127) solution transformed into the gel phase, as verified by the G′ value surpassing the corresponding G″ value. The crossover point of G′ and G″ known as the gelation temperature was about 29 °C, which was slightly higher than 24.5 °C obtained from the test tube inverting method above. This may be explained by the fact that the Poly(F127) solution became viscous upon heating and the fluidity could hardly be visually observed at 24.5 °C or above (Cohn et al., 2003).

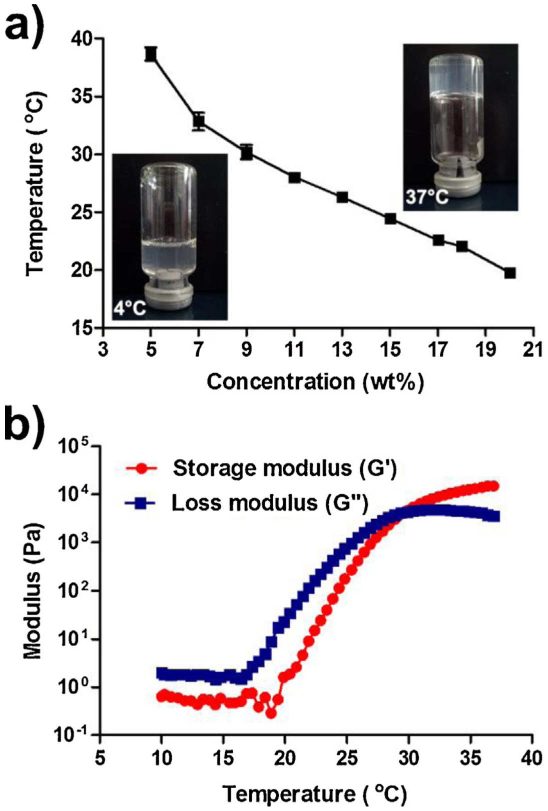

Fig. 3. (a) Sol-gel transition diagram of the Poly(F127) hydrogel at different concentrations determined using the tube inversion method ($n = 3$). Inset: optical images of the Poly(F127) hydrogel at 4 and 37 °C. (b) Rheological temperature sweep of the Poly(F127) hydrogel at the concentration of 15 wt%.

The PEGylated GNRs and PTX-M were simultaneously incorporated within the Poly(F127) hydrogel by a "cold method", in which both of them could be added on demand and uniformly dispersed in the matrix (Lin et al., 2014). The resulting hydrogel, PTX-M/GNR/gel was semi-transparent and deep red without any visible precipitate or aggregate (Supplementary Fig. S4b). Of note, the incorporation of the PEGylated GNRs and PTX-M had no significant influence on the sol-gel transition temperature, rheological properties and mechanical strength of the Poly(F127) hydrogel (Supplementary Fig. S4a,c,d). The as-prepared nanocomposite hydrogels were stored at room temperature, and ice-bathed before injection.

3.4. Photothermal conversion performance of nanocomposite hydrogel

To evaluate the *in vivo* photothermal conversion of nanocomposite hydrogel, the Heps-bearing mice were intratumorally injected with PTX-M/GNR/gel, and the temperature was monitored using a thermocouple needle inserted in the center of the tumor under 10 min of a 808 nm laser irradiation at a power intensity of 1.34 W/cm^2 or 2 W/cm^2. The temperature increased rapidly during the first 2 min followed by a steady-stated equilibrium. Under the laser irradiation of 1.34 W/cm^2, PTX-M/GNR/gel at the Au concentration of 21.6, 43.2 and 86.4 μg/mL resulted in a steady-stated temperature (T_{ss}) of 48.1 °C, 50.3 °C and 54.2 °C, respectively (Supplementary Fig. S5a), while under the laser irradiation of 2 W/cm^2, T_{ss} rose to 56.0 °C, 61.8 °C and 69.5 °C, respectively (Fig. 4a). At identical Au concentration and laser power intensity, the tumors treated with PTX-M/GNR/gel showed similar temperature increase profiles compared to that of the tumor treated with GNR/gel, suggesting that PTX-M in the hydrogel matrix had no effect on

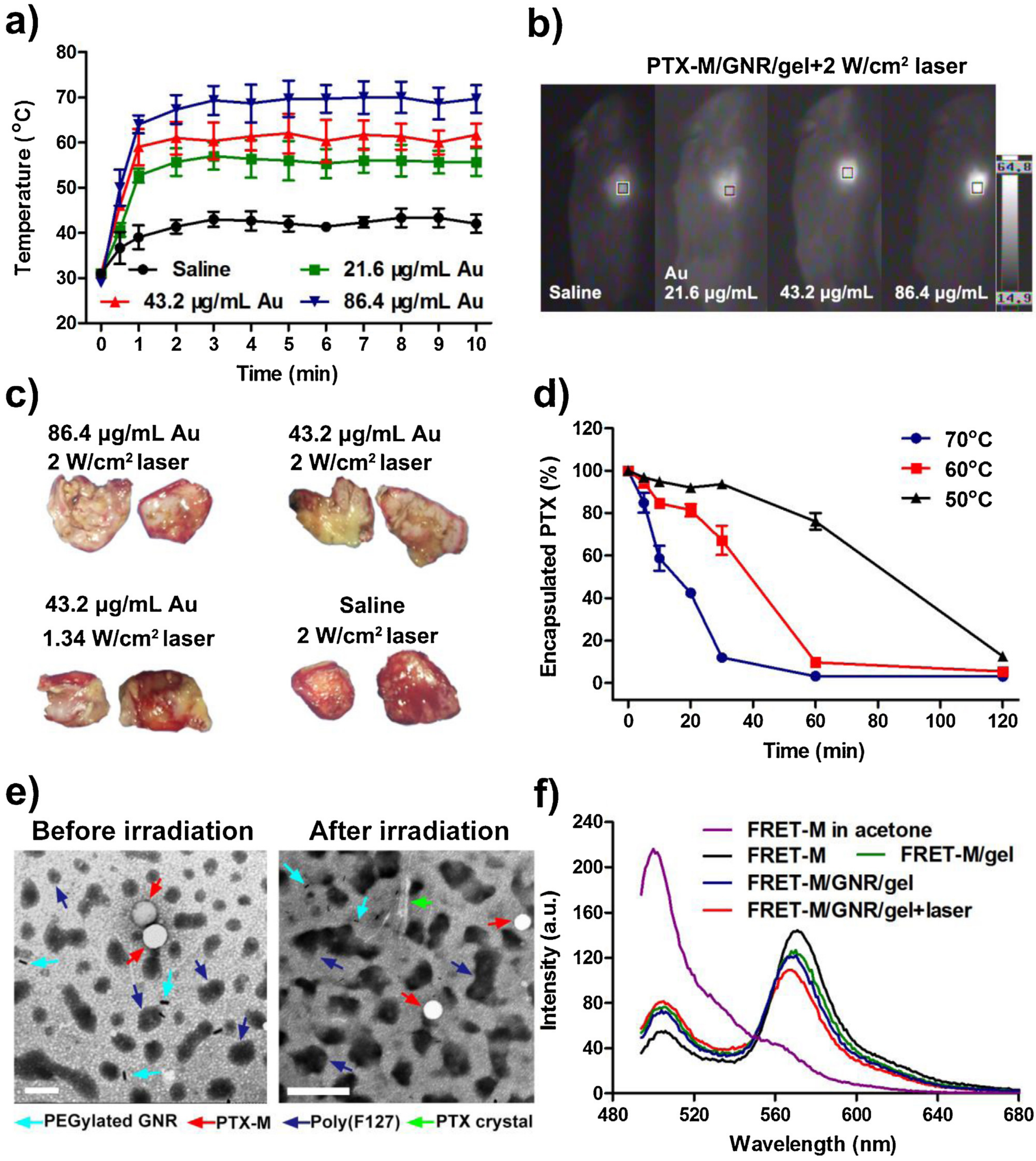

Fig. 4. (a) Temperatures increase profiles of the Heps tumor injected with PTX-M/GNR/gel at different Au concentrations under 10 min of 2 W/cm^2 laser irradiation. The temperature was measured with a thermocouple needle inserted into the center of tumor ($n = 3$). (b) Representative thermographs of the Heps tumor-bearing mice treated with PTX-M/GNR/gel at different Au concentrations under 10 min of 2 W/cm^2 laser irradiation, images were captured when the temperature of tumor region reached steady-state equilibrium. (c) Images of the TTC-stained tumor after treatment with PTX-M/GNR/gel under different conditions. Two tumor sections with different depth within the same tumor were collected. (d) PTX leakage of PTX-M under different temperatures over time. (e) TEM images of PTX-M/GNR/gel (43.2 μg/mL Au) before and after 10 min of 2 W/cm^2 laser irradiation. Scale bar: 200 nm (left) and 500 nm (right). (f) FRET-based characterization for the effect of photothermal treatment on the structural integrity of PTX-M in PTX-M/GNR/gel.

influencing the photothermal conversion efficiency of the PEGylated GNRs (Supplementary Fig. S6a,b). For the saline-treated tumor, T_{ss} was 37.9 °C and 41.5 °C at the laser power intensity of 1.34 W/cm^2 and 2 W/cm^2, respectively, both of which were not sufficient to induce coagulation necrosis (Nikfarjam et al., 2005). The changes of tumor temperature were also confirmed using an infrared thermographic camera. T_{ss} measured from thermal imaging was comparable to that measured using the thermal couple needle (Fig. 4b and Supplementary Fig. S5b, S6c, S6d). The regions of temperature elevation was mostly confined in the irradiated spot with a sharply-decreased temperature gradient extending to the adjacent non-irradiated region, suggesting that the heat could be selectively delivered to the tumor target and whereas spared the surrounding healthy tissue. These results suggested that T_{ss} was able to be flexibly tuned by adjusting either the Au concentration in the hydrogel or the laser power intensity to reach the thermal ablation temperature threshold (50–55 °C) (Burke et al., 2009), and moreover, the generated heat was primarily confined within the tumor region.

To evaluate the early-stage tumor damage induced by the photothermal treatment, the tumors were excised at 24 h post treatment, and stained with TTC. The viable tissue can be stained red as the essential mitochondrial enzymes of the respiratory chain reduced TTC into 1,3,5-triphenyl formazan (TPF) showing deep red color, while the ablated tissue retained its original color (Yang et al., 2010). As shown in Fig. 4c, for the saline-treated tumor under the laser irradiation of 2 W/cm^2, a large part of tumor tissue remained viable as they were stained red. The small portion of nonviable region may be mainly attributed to the spontaneous necrosis during the tumor growth rather than the laser-induced necrosis (Hoffmann et al., 2012). PTX-M/GNR/gel caused comparable tumor destruction with GNR/gel at the same Au concentration and laser power intensity (Fig. 4c and Supplementary Fig. S7, S8), which may be explained by the predominant thermal injury over a delayed cytotoxicity of PTX during the first 24 h post treatment. Apparent tumor damage, judged by extensive TTC-unstained region with occasionally bleeding, was observed in the tumor sections near the hydrogel–tumor interface at all three treatment conditions (Supplementary Fig. S8). However, viable residual tumor regions might also be identified in some tumor sections and their location was mostly found distal to the hydrogel and the skin surface (Fig. 4c and Supplementary Fig. S7), implying that heat generated

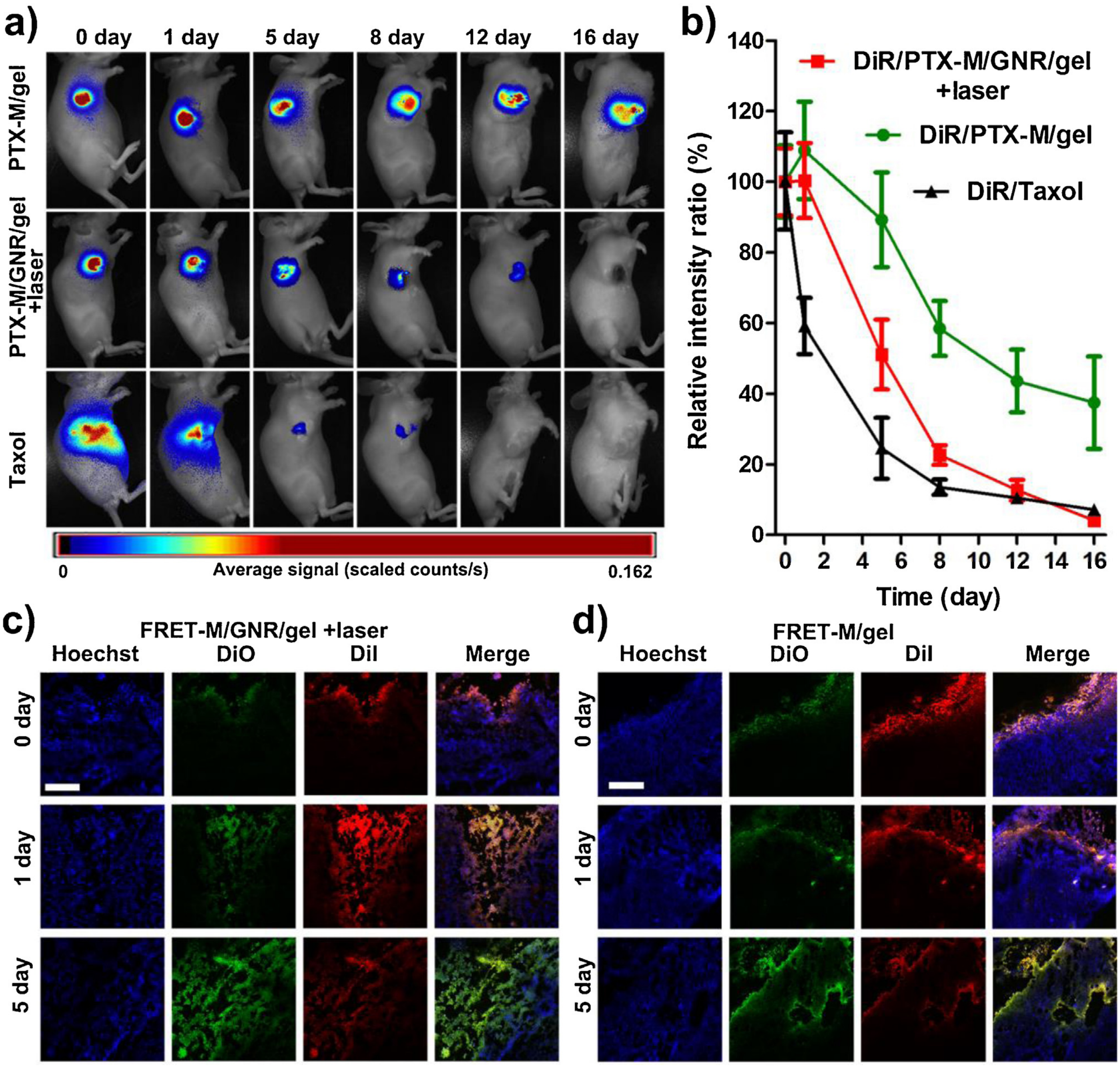

Fig. 5. (a) *In vivo* imaging of the Heps tumor-bearing mice treated with DiR/PTX-M/gel and DiR/PTX-M/GNR/gel (43.2 μg/mL Au) after 10 min of 2 W/cm^2 laser irradiation. DiR/Taxol was taken as a control. (b) Change in the relative intensity ratio of the DiR signal at the tumor region in the mice receiving the corresponding treatments. (c, d) Confocal images of the tumor sections collected from the Heps tumor-bearing mice treated with FRET-M/GNR/gel + laser (c) and FRET-M/gel (d) for different time. Nuclei were stained with Hoechst 33342. The DiO and DiI signals were simultaneously excited at 484 nm. Scale bar: 200 μm. (For interpretation of the references to color in this figure legend, the reader is referred to the web version of this article.)

from the GNR-containing hydrogel was not sufficiently transmitted to some portions of the tumor. Of note, the extent of tumor damage resulting from the treatment with 43.2 μg/mL Au and 2 W/cm^2 laser (corresponding T_{ss} = 60 °C) was not always enhanced compared to that of the treatment with 86.4 μg/mL Au and 2 W/cm^2 laser (corresponding T_{ss} = 70 °C). The uneven thermal damage could attributed to the heterogeneous temperature distribution: firstly, since the temperature decreased with the longer distance away from the hydrogel–tumor interface, the tumor cells located at the periphery distal to the hydrogel were not subjected to the ablative temperature; secondly, as most of the incident NIR light might be absorbed by the PEGylated GNRs in the top layers of the hydrogel due to the relatively high adsorption coefficients of GNRs, the increased Au concentration or laser power intensity resulted in a rapid rise in T_{ss} and the surface temperature but a less profound increment of the temperature deep in the tumor tissue (Elliott et al., 2007; Hirsch et al., 2003; Jong et al., 2011; Soni et al., 2014). These results indicated that the GNR-mediated photothermal treatment resulted in the heterogeneous and potentially incomplete heating within the tumors.

Next, the thermal stability of PTX-M was investigated, since PTX-M in PTX-M/GNR/gel underwent an acute temperature changes for a period of time upon the laser irradiation. When incubated at high temperature, the drug leakage of the PTX-M suspension was dramatically accelerated (Fig. 4d), which showed a concomitant increase with the temperature. Of note, the percentage of the remaining encapsulated PTX was about 85% after 10 min of incubation at 60 °C, the corresponding T_{ss} generated at 43.2 μg/mL Au and 2 W/cm^2 laser, indicating that most of PTX-M remained intact under this applied laser irradiation condition for photothermal therapy. The intact PTX-M was clearly observed by TEM after PTX-M/GNR/gel was exposed to laser irradiation at 2 W/cm^2 for 10 min (Fig. 4e), although a few of needle-like PTX crystals was formed due to the leakage of PTX from a small part of PTX-M. In addition, the förster resonance energy transfer (FRET)-based investigation were performed to further confirm the integrity of

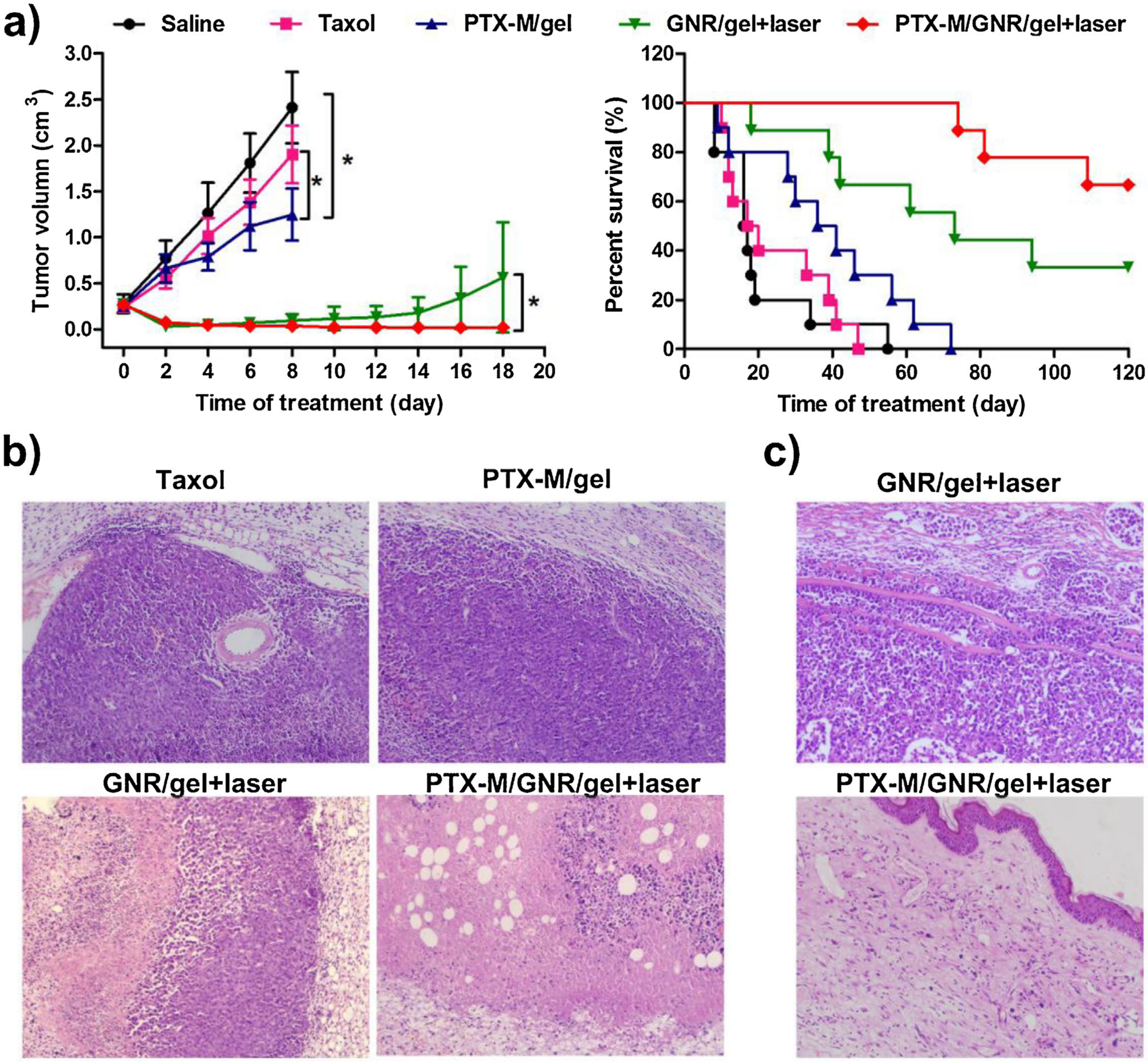

Fig. 6. (a) Tumor growth (left) and survival (right) of the Heps tumor-bearing mice after single intratumoral injection of saline, Taxol (20 mg/kg PTX), PTX-M (20 mg/kg PTX), GNR/gel (43.2 μg/mL Au) + laser (2 W/cm^2, 10 min), PTX-M/GNR/gel (43.2 μg/mL Au, 20 mg/kg PTX) + laser (2 W/cm^2, 10 min) (n = 9 or 10). (b) Representative images of the HE-stained tumor sections collected from the mice at 18 days after different treatments. (c) Representative images of the HE-stained tissue sections from the mice at 2 months after different treatments. Images were taken at 200× magnification.

PTX-M in PTX-M/GNR/gel after photothermal treatment (Fig. 4f) (Chen et al., 2008). A hydrophobic FRET pair, DIO as donor and DiI as acceptor, was physically encapsulated into PTX-M, namely FRET-M. The fluorescence spectra of FRET-M in water and acetone were first measured with the excitation of DiO at 484 nm. The proximate distance between DiO and DiI inside the intact micelles in water resulted an efficient FRET occurrence with a high FRET ratio ($I_{DiI}/(I_{DiI}+I_{DiO})$) of 0.72, where I_{DiI} and I_{DiO} are the fluorescence intensities of DiI at 570 nm and DiO at 502 nm, respectively. In sharp contrast, the FRET ratio of FRET-M in acetone dropped to 0.15, which resulted from the structural decomposition of FRET-M by the organic solvent and therefore the release of the two probes from the micelles. The FRET ratio was about 0.64 after incorporating FRET-M into the Poly(F127) hydrogel matrix, while after the laser irradiation of 2 W/cm^2 for 10 min, the FRET ratio decreased to 0.57, which was much higher than that in the decomposed state, indicating that FRET-M retained their structural integrity with cargos preserved in the micelles. Taken together, although the drug release from the micelles was accelerated under the ablative temperature range, most of PTX-M remained the structural integrity with the encapsulated drug for efficiently killing the residual tumor cells after photothermal treatment.

3.5. Tumor retention of nanocomposite hydrogel

PTX-M/GNR/gel acted as a localized drug depot in the tumor region, and the chemotherapeutic potential was relevant to local drug concentration, *in vivo* retention/release behavior and spatial distribution of drug (Wolinsky et al., 2012). The application of a long-term sustained release drug implant ensured a prolonged exposure of the tumor tissue to drugs and meanwhile maintained the therapeutic concentration, which contributed to the local tumor control.

To estimate the real-time tumor retention property of the nanocomposite hydrogels, we first incorporated DiR-labeled PTX-M (DiR/PTX-M) instead of PTX-M with the PEGylated GNRs into the Poly(F127) hydrogel matrix (designated as DiR/PTX-M/GNR/gel). DiR/PTX-M/gel and DiR-labeled Taxol (DiR/Taxol) were taken as control. The Heps-bearing mice were intratumorally injected with DiR-labeled formulations, followed by the non-invasive NIR imaging. As shown in Fig. 5a, DiR/Taxol showed poor tumor retention capability. The NIR signal was widely spread at the tumor and the surrounding region immediately after injection due to the rapid diffusion of DiR/Taxol away from the injection site, and the NIR signal intensity of the tumor region decreased rapidly within the first 5 days and almost completely disappeared after 8 days. By comparison, the hydrogel-based formulations showed a prolonged retention in the tumor site. The DiR signal was distributed mostly in the tumor region during the tested time period, and attenuated much more slowly than that of DiR/Taxol. The decay of the DiR signal of DiR/PTX-M/GNR/gel after laser irradiation in the tumor region was faster than that of DiR/PTX-M/gel group, indicating that the elimination of DiR from tumor was accelerated after photothermal treatment, which was potentially due to the expedited degradation of the hydrogel matrix and the promoted drug diffusion in the ablated tissue (Qian et al., 2003; Sun et al., 2011). The semi-quantitative results obtained from the region of interest analysis were in agreement with that of the *in vivo* imaging study (Fig. 5b), which substantiated that the hydrogel-based localized delivery showed enhanced tumor retention ability than Taxol.

To evaluate the cargo release and the integrity of the micelles in the hydrogel at the tumor site after laser irradiation, the FRET technique was applied. FRET-M/GNR/gel was intratumorally injected into the Heps-bearing mice, and the FRET signals in the tumor sections collected from the mice were detected over time after irradiation treatment. The FRET signal in the tumor displayed a similar change between FRET-M/GNR/gel and FRET-M/gel (Fig. 5c,d). At 0 and 1 day after treatment, a strong DiI signal (red) with a relatively weak DiO signal (green) was observed, suggesting a large majority of micelles remained intact in the tumor after irradiation treatment. As time increased to 5 days, a reduction of the FRET ratio as evidenced by the increased DiO signal and decreased DiI signal was detected, which could be attributed to the release of the FRET dyes from the micelles within the tumor. In contrast, although the FRET signal was visualized within the early time period after intratumoral injection of the FRET-M solution, both of the DiO and DiI signals rapidly decreased and were hardly detected at 5 days after injection (Supplementary Fig. S9), indicating the poor retention capability of the micelles without the support of the hydrogel matrix.

3.6. In vivo *antitumor efficacy*

The *in vivo* antitumor efficacy of PTX-M/GNR/gel mediated combination photothermal–chemotherapy was investigated on the xenograft Heps tumor model. The Heps-bearing mice were intratumorally injected with different formulations following the arranged protocol (Supplementary Table S2). There was no significant difference in the mean tumor volumes among the groups at the onset of treatments (*c.a.* 0.3 cm^3). The tumor growth and overall survival for each group were monitored (Fig. 6a).

The tumor of the mice treated with saline grew rapidly. The tumor volume increased to about 2.4 cm^3 at 8 days post treatment, and all the mice died within 55 days with a median survival of 17 days. Treatment with Taxol presented transient inhibition on the tumor growth. The tumor volume increased to 1.9 cm^3 at 8 days. However, all the mice died within 47 days with a median survival of 19 days, which did not remarkably prolong the survival compared to the treatment with saline. PTX-M/gel showed significant effect on inhibiting the tumor growth, which elevated the median survival to 39 days. The enhanced therapeutic efficacy of PTX-M/gel compared to Taxol resulted mainly from the prolonged drug retention in the tumor region, but still was not able to regress the tumor growth (Supplementary Fig. S10a), which was probably due to the suboptimal intratumoral drug and the limited drug diffusion from the micelle/hydrogel system to the whole fast-growing tumor mass. The failure in regressing tumor growth by Taxol and PTX-M/gel was evident by the histological examination (Fig. 6b). The hematoxylin-eosin (HE) stained tumor displayed the thriving tumor growth in the tumor mass at 18 days post treatment.

More significantly, all the mice treated with GNR/gel or PTX-M/GNR/gel under laser irradiation developed eschars at treatment site, and experienced substantial tumor regression during the first week post treatment. PTX-M/GNR/gel + laser showed superior antitumor activity than GNR/gel + laser (Fig. 6a and Supplementary Fig. S10a,b). Within 18 days post treatment, four of the nine mice treated with GNR/gel + laser sequentially experienced tumor regrowth, while none of the mice treated with PTX-M/GNR/gel + laser showed any sign of tumor relapse. As shown in Fig. 6b, the tumor treated with GNR/gel + laser showed extensive necrosis region, but large numbers of residual viable tumor cells could be detected in the periphery at 18 days post treatment. By comparison, treatment with PTX-M/GNR/gel + laser resulted in only few scattered tumor cells. The apparent regrowth of tumor in the GNR/gel + laser treated mice was observed, compared to the PTX-M/GNR/gel + laser treated one (Supplementary Fig. S10b). Within 2 months after treatment, the incidence of tumor regrowth increased to the ratio of six to nine mice treated with GNR/gel + laser, while still no evidence of tumor regrowth was found in the mice treated with PTX-M/GNR/gel + laser, which was also confirmed by the histological examination (Fig. 6c). The median survival of the mice treated with GNR/gel + laser was 73 days. Note that although three of the nine mice treated with PTX-M/GNR/gel + laser underwent tumor recurrence after 2 months post treatment, the others showed extremely improved survival due to complete treatment response, as substantiated by no death during the studied time period of 4 months. These data suggested that PTX-GNR/gel + laser integrating with photothermal therapy and chemotherapy was more potent in eliminating the residue tumor cells and achieving improved completeness of tumor damage.

3.7. Safety evaluation of OSPC/GNR/gel

In vitro safety evaluation against HepG 2 cells and L02 cells, OSPC/GNR/gel did not significantly affect the viability of both cells in the studied concentration range (Supplementary Fig. S11). In *in vivo* safety evaluation, the main tissues/organs of the mice receiving subcutaneous dorsal injection of OSPC/GNR/gel showed no pathological difference in comparison with the non-treated mice, including skin (Supplementary S12) as well as heart, liver, spleen, lung, kidney (Supplementary Fig. S13).

4. Conclusion

In summary, we developed PTX-M/GNR/gel for combined PTA and localized chemotherapy, in which both the PEGylated GNRs and PTX-M could be uniformly and dose-controlled incorporated. PTX-M/GNR/gel could be injected intratumorally, and immobilized in the tumor region due to the thermal-gelling property of Poly(F127) matrix, which rendered the tumor-specific heating with tunable thermal dose by adjusting the amount of the PEGylated GNRs and the power intensity of the laser. PTX-M/GNR/gel also acted as sustained and localized drug depot that could liberate PTX-M into tumor tissue to eliminate the residual tumors cells that survived the GNR-mediated photothermal treatment due to the heterogeneous temperature distribution, thereby improving the completeness of the tumor ablation and finally contributing to a delay and even elimination of tumor recurrence.

Acknowledgements

This work was supported by the National Natural Science Foundation of China (81473153, 81273468), National Basic Research Program of China (2015CB755500), State Key Laboratory of Natural Medicines at China Pharmaceutical University (SKLNMZZCX201401), 111 Project from the Ministry of Education of China and the State Administration of Foreign Expert Affairs of China (no. 111-2-07). This work was also supported by the Jiangsu Specially-Appointed Professors Program, the CPU High-Level Talent Program and the start-up package from CPU to R.M.

Appendix A. Supplementary data

Supplementary data associated with this article can be found, in the online version, at http://dx.doi.org/10.1016/j.ijpharm.2015.11.032.

References

Ahmed, M., Moussa, M., Goldberg, S.N., 2012. Synergy in cancer treatment between liposomal chemotherapeutics and thermal ablation. Chem. Phys. Lipids 165, 424–437.

Alkilany, A.M., Thompson, L.B., Boulos, S.P., Sisco, P.N., Murphy, C.J., 2012. Gold nanorods:their potential for photothermal therapeutics and drug delivery, tempered by the complexity of their biological interactions. Adv. Drug Deliv. Rev. 64, 190–199.

Bhatia, S.N., Karl, D.L., Yoon, S.S., Zhang, A.Y., Bagley, A.F., Lin, K.Y., 2010. Gold nanorod photothermal therapy in a genetically engineered mouse model of soft tissue sarcoma. Nano Life 1, 277–287.

Burke, A., Ding, X., Singh, R., Kraft, R.A., Levi-Polyachenko, N., Rylander, M.N., Szot, C., Buchanan, C., Whitney, J., Fisher, J., Hatcher, H.C., D'Agostino, R., Kock, N.D., Ajayan, P.M., Carroll, D.L., Akman, S., Torti, F.M., Torti, S.V., 2009. Long-term survival following a single treatment of kidney tumors with multiwalled carbon nanotubes and near-infrared radiation. Proc. Natl. Acad. Sci. U. S. A. 106, 12897–12902.

Chauhan, V.P., Stylianopoulos, T., Boucher, Y., Jain, R.K., 2011. Delivery of molecular and nanoscale medicine to tumors: transport barriers and strategies. Annu. Rev. Chem. Biomol. Eng. 2, 281–298.

Chen, H., Kim, S., Li, L., Wang, S., Park, K., Cheng, J., 2008. Release of hydrophobic molecules from polymer micelles into cell membranes revealed by Förster resonance energy transfer imaging. Proc. Natl. Acad. Sci. U. S. A. 105, 6596–6601.

Chen, H., Shao, L., Li, Q., Wang, J., 2013a. Gold nanorods and their plasmonic properties. Chem. Soc. Rev. 42, 2679–2724.

Chen, Y., Wu, H., Sun, J., Dong, G., Wang, T., 2013b. Injectable and thermoresponsive self-assembled nanocomposite hydrogel for long-term anticancer drug delivery. Langmuir 29, 3721–3729.

Cohn, D., Sosnik, A., Levy, A., 2003. Improved reverse thermo-responsive polymeric systems. Biomaterials 24, 3707–3714.

Dickerson, E.B., Dreaden, E.C., Huang, X., El-Sayed, I.H., Chu, H., Pushpanketh, S., McDonald, J.F., El-Sayed, M.A., 2008. Gold nanorod assisted near-infrared plasmonic photothermal therapy (PPTT) of squamous cell carcinoma in mice. Cancer Lett. 269, 57–66.

Elliott, A.M., Stafford, R.J., Schwartz, J., Wang, J., Shetty, A.M., Bourgoyne, C., O'Neal, P., Hazle, J.D., 2007. Laser-induced thermal response and characterization of nanoparticles for cancer treatment using magnetic resonance thermal imaging. Med. Phys. 34, 3102–3108.

Hirsch, L.R., Stafford, R.J., Bankson, J.A., Sershen, S.R., Rivera, B., Price, R.E., Hazle, J.D., Halas, N.J., West, J.L., 2003. Nanoshell-mediated near-infrared thermal therapy of tumors under magnetic resonance guidance. Proc. Natl. Acad. Sci. U. S. A. 100, 13549–13554.

Hoffmann, C.O.M., Rosenberg, C., Linder, A., Hosten, N., 2012. Residual tumor after laser ablation of human non-small-cell lung cancer demonstrated by ex vivo staining: correlation with invasive temperature measurements. Magn. Reson. Mater. Phys. Biol. Med. 25, 63–74.

Huang, X., Jain, P.K., El-Sayed, I.H., El-Sayed, M.A., 2008. Plasmonic photothermal therapy (PPTT) using gold nanoparticles. Lasers Med. Sci. 23, 217–228.

Huang, X., Neretina, S., El-Sayed, M.A., 2009. Gold nanorods: from synthesis and properties to biological and biomedical applications. Adv. Mater. 21, 4880–4910.

Issels, R.D., 2008. Hyperthermia adds to chemotherapy. Eur. J. Cancer 44, 2546–2554.

Jin, X., Mo, R., Ding, Y., Zheng, W., Zhang, C., 2014. Paclitaxel-loaded *N*-octyl-*O*-sulfate chitosan micelles for superior cancer therapeutic efficacy and overcoming drug resistance. Mol. Pharm. 11, 145–157.

Jong, B., Kim, Y.S., Choi, Y., 2011. Effects of gold nanorod concentration on the depth-related temperature increase during hyperthermic ablation. Small 7, 265–270.

Kennedy, L.C., Bickford, L.R., Lewinski, N.A., Coughlin, A.J., Hu, Y., Day, E.S., West, J.L., Drezek, R.A., 2011. A new era for cancer treatment: gold-nanoparticle-mediated thermal therapies. Small 7, 169–183.

Khlebtsov, N., Dykman, L., 2011. Biodistribution and toxicity of engineered gold nanoparticles: a review of *in vitro* and *in vivo* studies. Chem. Soc. Rev. 40, 1647–1671.

Le Renard, P.E., Jordan, O., Faes, A., Petri-Fink, A., Hofmann, H., Rüfenacht, D., Bosman, F., Buchegger, F., Doelker, E., 2010. The *in vivo* performance of magnetic particle-loaded injectable, *in situ* gelling, carriers for the delivery of local hyperthermia. Biomaterials 31, 691–705.

Li, W., Zhang, X., Zhou, M., Tian, B., Yu, C., Jie, J., Hao, X., Zhang, X., 2014. Functional core/shell drug nanoparticles for highly effective synergistic cancer therapy. Adv. Healthcare Mater. 3, 1475–1485.

Liao, H., Hafner, J.H., 2005. Gold nanorod bioconjugates. Chem. Mater. 17, 4636–4641.

Lin, Z., Gao, W., Hu, H., Ma, K., He, B., Dai, W., Wang, X., Wang, J., Zhang, X., Zhang, Q., 2014. Novel thermo-sensitive hydrogel system with paclitaxel nanocrystals: high drug-loading, sustained drug release and extended local retention guaranteeing better efficacy and lower toxicity. J. Control. Release 174, 161–170.

Liu, Y., Lu, W., Wang, J., Zhang, X., Zhang, H., Wang, X., Zhou, T., Zhang, Q., 2007. Controlled delivery of recombinant hirudin based on thermo-sensitive Pluronic® F127 hydrogel for subcutaneous administration: In vitro and *in vivo* characterization. J. Control. Release 117, 387–395.

Lu, W., Melancon, M.P., Xiong, C., Huang, Q., Elliott, A., Song, S., Zhang, R., Flores, L.G., Gelovani, J.G., Wang, L.V., Ku, G., Stafford, R.J., Li, C., 2011. Effects of photoacoustic imaging and photothermal ablation therapy mediated by targeted hollow gold nanospheres in an orthotopic mouse xenograft model of glioma. Cancer Res. 71, 6116–6121.

Meenach, S.A., Hilt, J.Z., Anderson, K.W., 2010. Poly(ethylene glycol)-based magnetic hydrogel nanocomposites for hyperthermia cancer therapy. Acta Biomater. 6, 1039–1046.

Mo, R., Jiang, T., Gu, Z., 2014. Enhanced anticancer efficacy by ATP-mediated liposomal drug delivery. Angew. Chem. Int. Ed. 53, 5815–5820.

Mo, R., Jin, X., Li, N., Ju, C., Sun, M., Zhang, C., Ping, Q., 2011. The mechanism of enhancement on oral absorption of paclitaxel by *N*-octyl-*O*-sulfate chitosan micelles. Biomaterials 32, 4609–4620.

Mooney, R., Roma, L., Zhao, D., Van Haute, D., Garcia, E., Kim, S.U., Annala, A.J., Aboody, K.S., Berlin, J.M., 2014. Neural stem cell-mediated intratumoral delivery of gold nanorods improves photothermal therapy. ACS Nano 8, 12450–12460.

Ni, W., Kou, X., Yang, Z., Wang, J., 2008. Tailoring longitudinal surface plasmon wavelengths, scattering and absorption cross sections of gold nanorods. ACS Nano 2, 677–686.

Nikfarjam, M., Muralidharan, V., Christophi, C., 2005. Mechanisms of Focal Heat Destruction of Liver Tumors. J. Surg. Res. 127, 208–223.

Oliva, N., Unterman, S., Zhang, Y., Conde, J., Song, H.S., Artzi, N., 2015. Personalizing biomaterials for precision nanomedicine considering the local tissue microenvironment. Adv. Healthcare Mater. 4, 1584–1599.

Qian, F., Stowe, N., Liu, E.H., Saidel, G.M., Gao, J., 2003. Quantification of *in vivo* doxorubicin transport from PLGA millirods in thermoablated rat livers. J. Control. Release 91, 157–166.

Qin, Z., Bischof, J.C., 2012. Thermophysical and biological responses of gold nanoparticle laser heating. Chem. Soc. Rev. 41, 1191–1217.

Redolfi Riva, E., Desii, A., Sinibaldi, E., Ciofani, G., Piazza, V., Mazzolai, B., Mattoli, V., 2014. Gold nanoshell/polysaccharide nanofilm for controlled laser-assisted tissue thermal ablation. ACS Nano 8, 5552–5563.

Ren, F., Bhana, S., Norman, D.D., Johnson, J., Xu, L., Baker, D.L., Parrill, A.L., Huang, X., 2013. Gold nanorods carrying paclitaxel for photothermal–chemotherapy of cancer. Bioconjug. Chem. 24, 376–386.

Shanmugam, V., Selvakumar, S., Yeh, C.S., 2014. Near-infrared light-responsive nanomaterials in cancer therapeutics. Chem. Soc. Rev. 43, 6254–6287.

Shenoi, M.M., Shah, N.B., Griffin, R.J., Vercellotti, G.M., Bischof, J.C., 2011. Nanoparticle preconditioning for enhanced thermal therapies in cancer. Nanomedicine 6, 545–563.

Singh, R., Torti, S.V., 2013. Carbon nanotubes in hyperthermia therapy. Adv. Drug Deliv. Rev. 65, 2045–2060.

Soni, S., Tyagi, H., Taylor, R.A., Kumar, A., 2014. Investigation on nanoparticle distribution for thermal ablation of a tumour subjected to nanoparticle assisted thermal therapy. J. Therm. Biol. 43, 70–80.

Sun, G., Zhang, X., Shen, Y.I., Sebastian, R., Dickinson, L.E., Fox-Talbot, K., Reinblatt, M., Steenbergen, C., Harmon, J.W., Gerecht, S., 2011. Dextran hydrogel scaffolds enhance angiogenic responses and promote complete skin regeneration during burn wound healing. Proc. Natl. Acad. Sci. U. S. A. 108, 20976–20981.

Sun, T., Wang, Y., Wang, Y., Xu, J., Zhao, X., Vangveravong, S., Mach, R.H., Xia, Y., 2014. Using SV119-gold nanocage conjugates to eradicate cancer stem cells through a combination of photothermal and chemo Therapies. Adv. Healthcare Mater. 3, 1283–1291.

Thakor, A.S., Gambhir, S.S., 2013. Nanooncology: the future of cancer diagnosis and therapy. Ca-Cancer J. Clin. 63, 395–418.

Vigderman, L., Khanal, B.P., Zubarev, E.R., 2012. Functional gold nanorods: synthesis, self-assembly, and sensing applications. Adv. Mater. 24, 4811–4841.

von Maltzahn, G., Park, J.-H., Agrawal, A., Bandaru, N.K., Das, S.K., Sailor, M.J., Bhatia, S.N., 2009. Computationally guided photothermal tumor therapy using long-circulating gold nanorod antennas. Cancer Res. 69, 3892–3900.

Weinberg, B.D., Blanco, E., Gao, J., 2008. Polymer implants for intratumoral drug delivery and cancer therapy. J. Pharm. Sci. 97, 1681–1702.

Wicki, A., Witzigmann, D., Balasubramanian, V., Huwyler, J., 2015. Nanomedicine in cancer therapy: challenges, opportunities, and clinical applications. J. Control. Release 200, 138–157.

Wiradharma, N., Khan, M., Tong, Y., Wang, S., Yang, Y., 2008. Self-assembled cationic peptide nanoparticles capable of inducing efficient gene expression in vitro. Adv. Funct. Mater. 18, 943–951.

Wolinsky, J.B., Colson, Y.L., Grinstaff, M.W., 2012. Local drug delivery strategies for cancer treatment: gels, nanoparticles, polymeric films, rods, and wafers. J. Control. Release 159, 14–26.

Xu, X., Meade, A., Bayazitoglu, Y., 2013. Feasibility of selective nanoparticle-assisted photothermal treatment for an embedded liver tumor. Lasers Med. Sci. 28, 1159–1168.

Yang, W., Ahmed, M., Elian, M., Hady, E.S.A., Levchenko, T.S., Sawant, R.R., Signoretti, S., Collins, M., Torchilin, V.P., Goldberg, S.N., 2010. Do liposomal apoptotic enhancers increase tumor coagulation and end-point survival in percutaneous radiofrequency ablation of tumors in a rat tumor model? Radiology 257, 685–696.

Yao, Z., Zhang, C., Ping, Q., Yu, L., 2007. A series of novel chitosan derivatives: Synthesis, characterization and micellar solubilization of paclitaxel. Carbohydr. Polym. 68, 781–792.